Cichocki, F., Merino, M. & Ahedo, E. (2018). Spacecraft-plasma-debris interaction in an ion beam shepherd mission. *Acta Astronautica*, vol. 146, p. 216–227.

DOI: 10.1016/j.actaastro.2018.02.030

Spacecraft-plasma-debris interaction in an ion beam shepherd mission

Filippo Cichocki, Mario Merino and Eduardo Ahedo

Universidad Carlos III de Madrid, Avenida de la Universidad, 30, 28911 Leganés, Madrid, Spain

E-mail: filippo.cichocki@uc3m.es

Keywords: plasma plumes, hybrid, particle-in-cell, ion-beam-shepherd, active-debris-removal, sputtering

Abstract. This paper presents a study of the interaction between a spacecraft, a plasma thruster plume and a free floating object, in the context of an active space debris removal mission based on the ion beam shepherd concept. The analysis is performed with the EP2PLUS hybrid code and includes the evaluation of the transferred force and torque to the target debris, its surface sputtering due to the impinging hypersonic ions, and the equivalent electric circuit of the spacecraft-plasma-debris interaction. The electric potential difference that builds up between the spacecraft and the debris, the ion backscattering and the backsputtering contamination of the shepherd satellite are evaluated for a nominal scenario. A sensitivity analysis is carried out to evaluate quantitatively the effects of electron thermodynamics, ambient plasma, heavy species collisions, and debris position.

1. Introduction

The space debris problem is becoming a serious threat for the future exploitation of low Earth orbits [1, 2, 3, 4], in particular the sunsynchronous and the polar ones. If the number of orbital objects continued to increase without control, the space debris density would reach a critical point, beyond which cascading collisions would cause an uncontrolled population growth, thus endangering space exploitation for generations (Kessler syndrome [1]). In any case, the actual space debris population is already having a non-negligible impact on operational mission costs, as frequent collision avoidance maneuvers are necessary to reduce the collision risks to acceptable levels. In order to tackle this serious issue, two remediation strategies can be followed: (I) common disposal strategies (e.g. internationally accepted laws that regulate the end of life of satellites) and (II) active debris removal (ADR) strategies, in which space debris objects are actively deorbited or repositioned. While being strictly necessary, the first approach is not enough to prevent the debris population from growing indefinitely, as suggested by recent research [2], so that the international community interest in ADR techniques is rapidly growing.

The ion beam shepherd (IBS) concept [5, 6, 7, 8, 9] is one such technique, in which the space debris object (or an asteroid in a deflection mission) is gradually relocated by the slowly pushing action of a hypersonic plasma plume, generated by a plasma thruster onboard a shepherd spacecraft. The IBS requires two thrusters: an impulse transfer thruster (ITT) to generate this plume, and an impulse compensation thruster (ICT), located on the other side of the spacecraft, to maintain formation flight with the target debris. This technique is contactless (a fixed security distance is maintained from the debris), and uses electric propulsion, thus being very efficient from the point of view of propellant consumption, especially in multi-target missions. This makes the IBS particularly appealing, when compared with other ADR techniques that involve capturing physically or docking with the uncooperative debris object and/or using chemical propulsion (e.g. the technique known as space tug).

Recent studies [5, 7, 8, 9, 10, 11, 12, 13] have focussed on assessing the efficiency and the feasibility of the IBS technique. By assuming a simplified plume and target interaction model, the fraction of ITT thrust transferred to the debris has been found to depend on different factors: the operational shepherding distance, the initial plume divergence angle at the thruster exit, and the ratio between the ion kinetic energy and the plume electrons thermal energy. In particular, the higher this ratio and the lower the initial plume divergence angle, the larger the transferred thrust.

Although the IBS is a relatively simple concept, the evaluation of some operational issues requires an advanced study of the plasma plume interaction between the IBS and the debris object. In particular, the following phenomena are critical, especially for long duration IBS missions (e.g. for multi-target missions):

- The ion backscattering flow: charge-exchange collisions, occurring near the thruster exit, produce a low energy ion population that is deflected back towards the satellite by the local electric field. This ion backscattering affects all electric propulsion missions and can produce erosion and/or contaminate sensitive spacecraft surfaces, such as the solar

arrays or some optical sensors, whose performance would degrade.

- The sputtered atom backflow from the target debris: the hypersonic plume ions are energetic enough to knock out atoms of the space debris object, which can then flow towards the spacecraft and represent an additional source of contamination.
- Electric charging effects: the emitted plasma plume connects electrically the spacecraft and the debris object (plasma bridge), and dominates the relative charging of the two objects. Other sources of electric charging are the backscattered ions (from CEX), the photoemission due to the incident light on the objects, the secondary electron emission, the ion bombardment emission, and the ambient plasma (both ions and electrons).

This study aims at evaluating quantitatively the above described phenomena, for the baseline IBS mission scenario of LEOSWEEP [14], a European Commission funded project aiming at designing and studying the feasibility of a demonstration IBS mission. Moreover, the force and torque transferred to the target debris are evaluated and compared with those obtained with simplified plume models, considered in previous studies. In order to perform such analyses, the simulation code EP2PLUS of Refs. [15] and [16] is used. This hybrid PIC-DSMC/fluid code treats ions and neutrals as macro-particles and electrons as a fluid, thus overcoming the computational disadvantages of full-PIC or fully-kinetic codes.

The rest of the paper is structured as follows. Sec. 2 introduces the simulation scenario and setup, the code capabilities, and the main modeling issues. Then, Sec. 3 describes and discusses the corresponding results, while Sec. 4 presents a sensitivity analysis. Finally, conclusions and future work are summarized in Sec. 5. A preliminary version of this work has been presented in Ref. [17].

2. Nominal IBS-plasma-debris scenario and model

2.1. IBS mission geometry and specifications

The nominal scenario considered for this study is the same as in Ref. [13], and features a 500 kg IBS spacecraft, a cubic target debris of 1.5 tons mass and 1.25 m spherical envelope radius, an overall de-orbiting maneuver of 300 km in 170 days (with 67% of daylight fraction). These specifications put a constraint on the minimum transferred force to the debris: $F_{\mathrm{ITT}} \geq 30$ mN. This force requirement has to be fulfilled for an operational distance between the ITT thruster and the target center of mass of 7 m.

The simulation geometry is described in Fig. 1 (a) and (b) and features an IBS with both thrusters and corresponding neutralizers. The solar panels are oriented with their normal at 90 deg with respect to the orbital plane ($x - z$ plane), a typical operational condition in sun-synchronous orbits with a local solar time at the ascending node equal to either 6AM or 6PM.

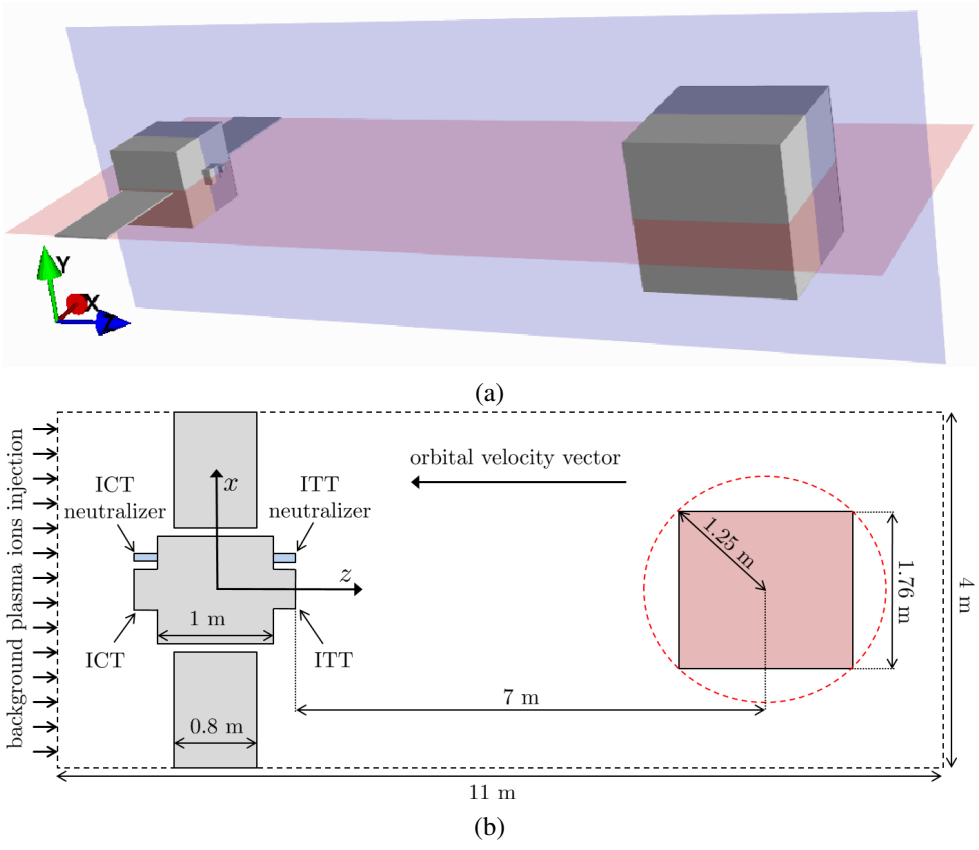

Figure 1: Simulation geometry for the IBS-plasma plume-debris interaction: (a) 3D rendering showing two important cross sections through the satellite center, $y = 0$ (in red) and $x = 0$ (in blue). (b) Schematic view of the $y = 0$ cross section showing the simulation objects size and the ambient ions injection direction. The thickness of the solar arrays along the y direction (towards the reader) is 4 cm, while the Sun is along the $+y$ direction. The cell size of the structured mesh is 2 cm along x and y, and 4 cm along z.

2.2. Simulation setup

The above defined IBS scenario is simulated with EP2PLUS, whose architecture and models are described in detail in Refs. [15, 16]; the following only presents an overview of the code main features and capabilities.

EP2PLUS is a 3D hybrid PIC-DSMC/fluid code, based on a structured mesh (either Cartesian or deformed non-uniform), in which ions and neutrals are treated as macro-particles of a PIC sub-model, and electrons as a fluid. The electron fluid model features weak collisionality and a fluid closure based on a polytropic equation of state, an assumption that has proven to retain the essential plume expansion physics, as demonstrated by comparison with both experiments [18, 19, 20, 21, 22, 23, 24, 25, 26], and kinetic simulations [27, 28, 29, 30, 31]. The code is capable of simulating (I) heavy particle collisions, such as charge-exchange (CEX) or single and multiple ionization collisions, (II) macro-particles interaction with either dielectric and conductive walls, (III) electric currents within the plasma and towards the objects walls, (IV) quasineutral and non-neutral regions (automatic subdivision of the simulation domain, with a non-linear Poisson solver for the latter non-neutral regions), and

Table 1: IBS simulation parameters for the nominal scenario. Applied voltages refer to the IBS ground. The thruster injection surfaces are circular with radius $R_0 = 8$ cm. The thruster ion velocity profiles are conical, with a cone vertex located inside the thruster.

Simulation parameter	**Units**	**Values**
Neutralizers keeper voltage	V	10
ITT/ICT last grid voltages	V	−100
ITT/ICT beam voltage	V	3500/1000
Doubly-charged to total ion current ratio for thrusters and neutralizers	%	9.1
ITT/ICT thruster mass flow rate	mg/s	0.566/1.293
ITT/ICT mass utilization efficiency	%	75/85
ITT injected Xe^+ profile	n/a	conical velocity ($R_0 = 8$ cm, $\alpha_0 = 7$ deg)
ICT injected Xe^+ profile	n/a	conical velocity ($R_0 = 8$ cm, $\alpha_0 = 35$ deg)
ITT injected Xe^{++} profile	n/a	conical velocity ($R_0 = 8$ cm, $\alpha_0 = 15$ deg)
ICT injected Xe^{++} profile	n/a	conical velocity ($R_0 = 8$ cm, $\alpha_0 = 40$ deg)
ITT/ICT injected Xe^+ temperature	eV	0.1
ITT/ICT injected Xe^{++} temperature	eV	0.2
ITT/ICT injected neutrals profile	n/a	flat
ITT/ICT inj. neutrals axial velocity	m/s	247
ITT/ICT injected neutrals temperature	eV	0.05
ITT/ICT neutralizers mass flow rate	mg/s	0.0566/0.0566
Neutralizer ion mass flow percentage	%	5.0
Neutralizer injected neutrals profile	n/a	flat
Neutralizer injected neutrals axial velocity	m/s	247
Neutralizer injected neutrals temperature	eV	0.05
Neutralizer injected Xe^+, Xe^{++} profile	n/a	thermal, Gaussian ($R_0 = 2$cm)
Neutralizer injected Xe^+ temperature	eV	0.2
Neutralizer injected Xe^{++} temperature	eV	0.4
Electron temperature at ITT thruster exit	eV	3.0
Electron polytropic cooling coefficient	n/a	1.15
Background plasma density (O^+ ions)	m^{-3}	$5 \cdot 10^{10}$
Background plasma temperature (O^+ ions)	eV	0.15
Background O^+ ions velocity	km/s	7.5
Target debris material	n/a	Al
Material walls accommodation coefficient	n/a	0.98
Material walls temperature	K	400.0
Simulation duration	s	$5.577 \cdot 10^{-3}$
PIC time step	s	$2.788 \cdot 10^{-7}$

(v) correct ion flux conditions at quasineutral material boundaries (with a Bohm condition forcing algorithm). A dedicated plasma sheath model and an equivalent circuit, which models the interaction of the simulation objects with the plasma, finally provide the correct boundary conditions for the electric potential and electron current density solvers.

The simulation parameters are summarized in Table 1. Four different heavy particle species are considered: the emitted ions Xe^+ and Xe^{++}, the emitted neutrals Xe, and the ambient ions O^+. The operational conditions of both thrusters are those minimizing the total

electric propulsion subsystem power, as shown in the optimization study of Ref. [13]. The ITT and ICT feature respectively a total mass flow of 0.566 and 1.293 mg/s, with a mass utilization efficiency (ratio between ion and total mass flow) of respectively 75 and 85 %. Both neutralizers feature a total mass flow of 0.0566 mg/s, and emit 95% of this mass flow as neutrals and the remaining 5% as either singly or doubly-charged ions. For both thrusters and neutralizers, 9.1% of the total emitted ion current is constituted by doubly-charged ions.

Xe neutrals are emitted by the thrusters and neutralizers at sonic conditions ($M = 1$), and they expand adiabatically with $\gamma = 5/3$ and a reference temperature of 0.05 eV. Regarding the thruster ions, both singly and doubly-charged ions are emitted, with a kinetic energy provided by their corresponding beam voltage (respectively 3500 and 1000 eV for the singly-charged ions emitted by the ITT and ICT). The injection profiles are nearly-Gaussian in density and conical in velocity (the divergence angle tangent increases linearly with the radius from the thruster axis), following the Ashkenazy-Fruchtman initial profile [11], with values for the outermost ion streamline radius R_0 and divergence angle α_0 shown in the table. The neutralizer ions, on the other hand, are emitted thermally with temperatures of 0.2 and 0.4 eV for, respectively, the singly and doubly-charged ions.

Finally, the background population of O^+ ions is assumed to be moving along the positive z direction, with a velocity comparable to the LEO orbital velocity (7.5 km/s), a temperature of 0.15 eV, and a density of $5 \cdot 10^{10}$ m^{-3}, which corresponds to an average plasma density at an altitude of 600 km. The flow direction of the injected ions is typical of a de-orbiting scenario, in which the shepherd spacecraft is ahead of the space debris along the orbit direction.

Regarding the heavy particle collisions, the considered model includes (I) resonant symmetric CEX collisions between the emitted Xe ions and neutrals (both Xe^+ + Xe and Xe^{++} + Xe), and (II) ionization collisions of different degrees, again only for the Xe species (Xe $\rightarrow$ Xe^+, Xe $\rightarrow$ Xe^{++} and Xe^+ $\rightarrow$ Xe^{++}). Collisions within the oxygen ambient ions population, the sputtered Al atoms population, and the cross-species collisions between these two species and the emitted Xe species, are neglected due to their mean free paths:: (I) Xe-O collisions have a mean free path $\lambda_c \sim 10^6$ km, and (II) Xe-Al collisions, at the very surface of the target debris (where Al density is highest), have a mean free path $\lambda_c \sim 10$ km, both much larger than the simulation domain ($\sim$ 10 m).

The electron temperature (3 eV) is fixed at a reference node located 8 cm downstream of the ITT thruster exit. The simulation duration is 5.6 ms with a time step of 0.28 μs, ensuring that the injected doubly-charged ions of the ITT (fastest particle species) cross less than 1 cell. As explained in Ref. [16], the code features both a quasineutral and a non-neutral solver. To speed up the simulation, thus quickly filling the simulation domain with particles, the first 15000 steps ($t < 4.18$ ms) are run with the quasineutral solver alone, while the non-neutral solver is activated afterwards.

2.3. Modeling the plasma-surface interaction

When a heavy particle hits a material surface, it can undergo two different processes: (I) a quick reflection (nearly specular) within the first atomic layers, with a backscattering

probability p_b, or (II) a partial/complete accommodation within the wall, in which the particle gradually loses memory of its impact direction and approaches a thermodynamic equilibrium with the lattice atoms, being finally re-emitted diffusely [32, 33, 34, 35]. Additionally, if the impacting particle kinetic energy is large enough to overcome the binding energy of the constituent atoms of the material lattice, it can also cause sputtering, which means that it knocks out a certain number of material atoms from its surface.

Both the sputtered particle distribution and the backscattering probability p_b of the incident particles generally depend on the impacting particle species, the surface material (e.g. its binding energy), the impact kinetic energy E_i (per elementary particle), and the impact angle α_i (angle between the impacting particle direction and the surface normal) [36, 37]. In the present study, the sputtered particle distribution has been modeled by defining: (I) the sputtering yield Y (number of sputtered atoms per impacting particle), (II) the emission mean energy $\bar{E}_s$ of the sputtered atoms, and (III) their angular distribution.

For a given impacting species and target material, Y, $\bar{E}_s$ and p_b, are 2D functions of the impact energy and angle, and have been evaluated with the software SRIM/TRIM [38] for a target debris made of aluminium and a plasma plume made of xenon ions (alternatively, simplified empirical models, like those of Refs. [36] and [37] can be used). As shown in Fig. 2 (a), the yield presents a maximum value at oblique incidence angles (around 75 deg) and grows with the impact energy. The sputtered atoms energy shown in Fig. 2 (b), on the other hand, grows monotonically with both the particle energy and impact angle. Finally, the backscattering probability, Fig. 2 (c), is practically independent of the impact energy and grows with the impact angle, being maximum at grazing incidence and zero for $\alpha_i < 45$ deg. For instance, the values of yield and mean sputtered atoms energy for the ITT singly-charged ions at 3500 eV of energy (refer to Table 1) and impacting at normal incidence, are respectively 2 and 14 eV, while the backscattering probability is almost zero.

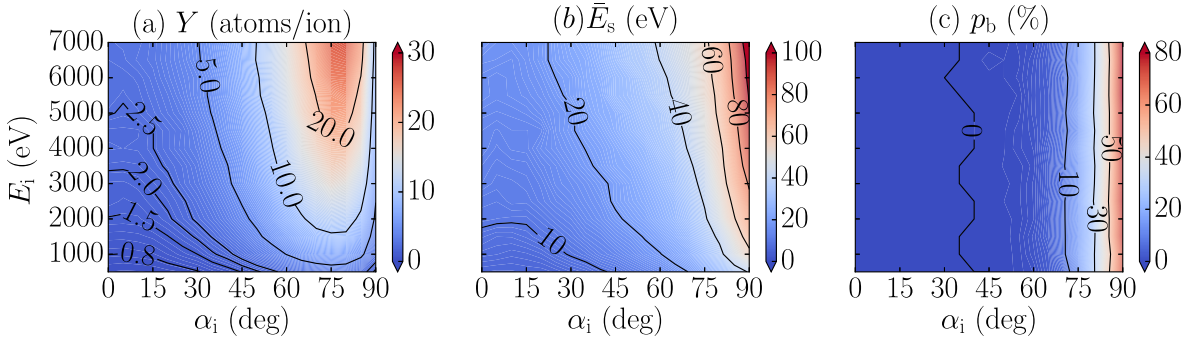

Figure 2: Sputtering properties for a hypersonic flow of Xe ions/atoms on an Al target, showing (a) the particle yield (i.e. the average number of sputtered atoms per incident particle), (b) the mean sputtered atoms emission energy, and (c) the incident particle backscattering probability.

The models for both the generation of sputtered atoms and the backscattering or accomodation processes of incident particles are described in detail in the Appendix. In particular, all impacting particles that are not backscattered, are re-emitted diffusely as neutrals, with a lower energy, that depends on their impacting kinetic energy, the wall

temperature and an energy accommodation coefficient α_W [33, 34, 35].

In the simulations, the detailed sputtering and backscattering parameters have been computed only for the plasma plume-target interaction. For the IBS surfaces, subject to the impact of particles with much lower energies, both the sputtering yield and the backscattering probability are zero. Finally, the sputtering effects of the ambient ions on the target debris are also neglected with respect to those of the impinging Xe ions, because (I) their density is $3-4$ orders of magnitude lower (at the target debris surface), and (II) the corresponding yield at their low energy (tens of eVs at most) is almost negligible.

2.4. Sheath solver and equivalent circuit of the shepherd spacecraft-debris system

Two types of material objects are considered: dielectric and conductive. The former are characterized by a local wall potential, resulting from the zero net current condition. The conductive objects, on the other hand, are iso-potential and can be represented as a single node in the equivalent electric circuit. A sheath model computes the boundary electric current density at the walls of conductive objects, as a function of their potential.

The equivalent circuit is shown in Fig. 3 for an IBS scenario, which features two sub-circuits: the spacecraft and the space debris. The spacecraft subcircuit is composed of the

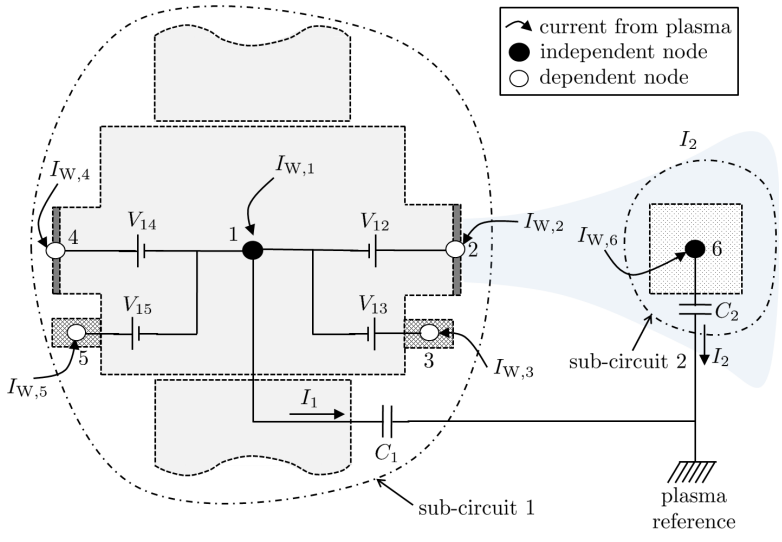

Figure 3: Equivalent circuit of the IBS spacecraft-target debris system

following conductive objects: the last grid of both ion thrusters (ITT and ICT), the neutralizer keepers, and the IBS ground, which consists of a cubic body, the ITT and ICT cases, and the bottom face of the solar array (e.g. the dark face, the illuminated face being modeled as a dielectric object, and, hence, not shown in the figure). The space debris sub-circuit only features the debris cubic body. As described in Ref. [16], the floating potential with respect to a plasma reference node of both sub-circuits is obtained as the time evolution of a capacitor voltage, in which the charging current is given by the sum of the electric currents I_W reaching the walls of each object. For the electric scheme of Fig. 3, this means that the IBS and target

nodes potentials, respectively ϕ_1 and ϕ_6, are obtained as:

$$\frac{\mathrm{d}\phi_1}{\mathrm{d}t} = \frac{\sum_{l=1}^{5} I_{\mathrm{W},l}}{C_1} \quad , \quad \frac{\mathrm{d}\phi_6}{\mathrm{d}t} = \frac{I_{\mathrm{W},6}}{C_2}. \tag{1}$$

Finally, the other object potentials and the inter-object currents of Fig. 3 are computed by solving the system of Kirchhoff laws for both currents and potentials, as shown in Ref. [16].

2.5. Computation of the transferred force and torque to the debris

The estimation of the total force and torque transferred to the target debris is of fundamental importance in the context of an IBS mission. While the ratio between transferred force and ITT thrust determines directly the technique efficiency, the tranferred torque is necessary to estimate the angular acceleration of the space debris. The present model is able to refine former calculations of the thrust and torque [5, 7, 8, 9, 12, 13, 39], considering the contributions from (I) linear momentum of impacting and emitted macro-particles (the latter contributing with a recoil effect), (II) electron linear momentum, and (III) electric forces. Therefore, the transferred force to a space debris surface element of area $\mathrm{d}S$ is given by:

$$\mathrm{d}\boldsymbol{F}_{\mathrm{target}} = \left[\dot{\boldsymbol{p}}_{\mathrm{in}} - \dot{\boldsymbol{p}}_{\mathrm{out}} - \left(p_{\mathrm{e}} + m_{\mathrm{e}} n_{\mathrm{e}} u_{\mathrm{e}\perp}^2\right)\mathbf{1}_{\perp} + \bar{\bar{\sigma}} \cdot \mathbf{1}_{\perp}\right]\mathrm{d}S, \tag{2}$$

where $\dot{\boldsymbol{p}}_{\mathrm{in}}$ and $\dot{\boldsymbol{p}}_{\mathrm{out}}$ represent the linear momentum vector flux of respectively the impacting and emitted macro-particles, $\mathbf{1}_{\perp}$ is the normal unit vector, oriented towards the plasma, $p_{\mathrm{e}} = n_{\mathrm{e}} T_{\mathrm{e}}$ is the electron pressure, $u_{\mathrm{e}\perp}$ is the electron fluid velocity perpendicular to the wall, and $\bar{\bar{\sigma}}$ is the electrostatic Maxwell stress tensor [40], with components $\sigma_{ij} = E_i E_j - \delta_{ij} E^2/2$. For conductive objects, the tangential electric field is zero, so that $\bar{\bar{\sigma}} \cdot \mathbf{1}_{\perp} = (1/2)\epsilon_0 E^2 \mathbf{1}_{\perp}$, and the electrostatic force becomes normal to the surface and directed towards the plasma.

The total transferred force can be obtained by summing the elementary contributions of Eq. 2, evaluated either at the material wall or at the plasma sheath edge, with the same numerical result. In fact, a change in the electron and ion momentum flux is compensated by an equal and opposite variation of the electric force. At a negative material wall (with respect to the plasma), the ion momentum flux (due to the sheath acceleration) and the electric suction force (towards the plasma) are higher than at the sheath edge, while the electron momentum flux is generally negligible, as shown in Table 3.

Finally, the elementary torque with respect to the target center of mass is computed as

$$\mathrm{d}\boldsymbol{\tau}_{\mathrm{target}} = \boldsymbol{r} \times \mathrm{d}\boldsymbol{F}_{\mathrm{target}}, \tag{3}$$

with $\boldsymbol{r}$ representing the radius from the target center of mass to each cell-face center.

3. Simulation results for the nominal IBS scenario

This section shows time-averaged values (over 100 time steps) of the steady-state reached at the end of the simulation, and obtained with the non-neutral solver. The electric potential ϕ relative to the IBS ground is shown on three different sections in Fig. 4 (a) to (c).

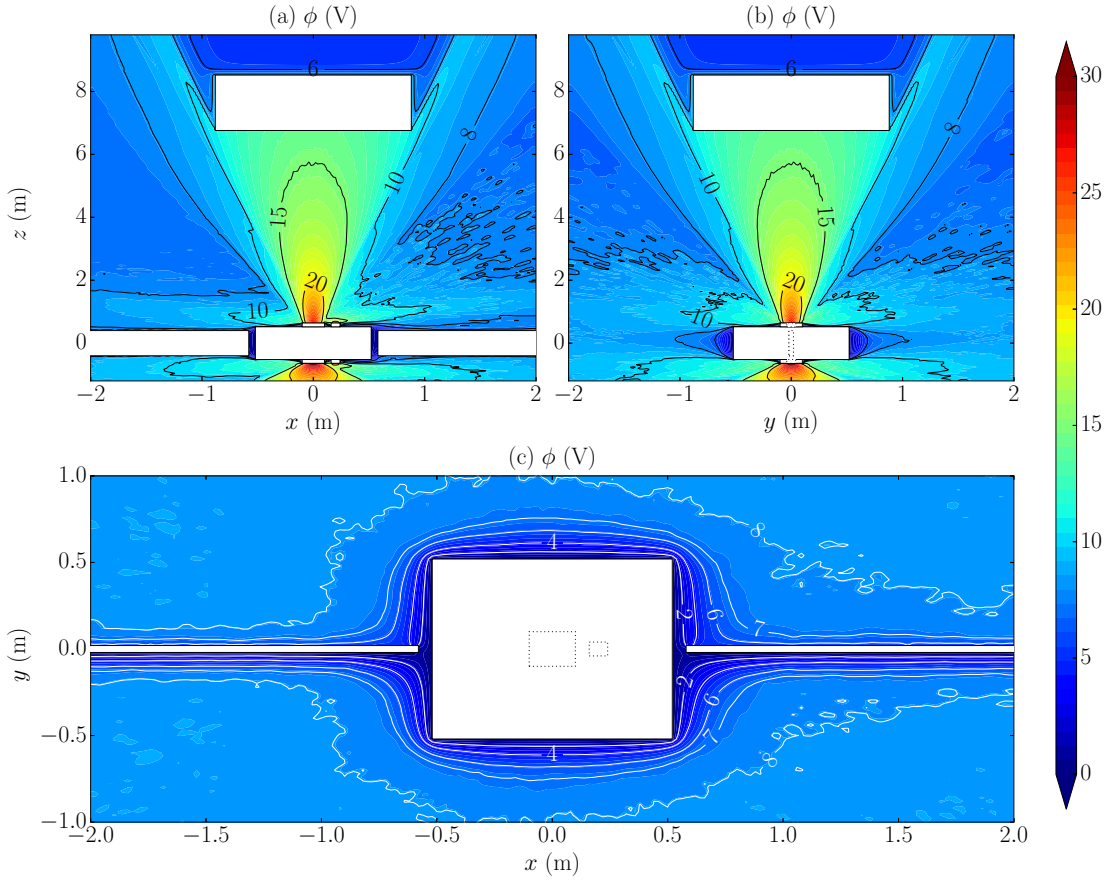

Figure 4: Nominal scenario results: electric potentials at (a) $y = 0$, (b) $x = 0$, and (c) $z = 0$. All planes pass through the geometric center of the satellite cubic body. The potential is relative to the IBS ground. The horizontal and vertical axes scales are different.

The effects of CEX ions and emitted plume of the neutralizers are clearly visible in Fig. 4 (a) ($y = 0$), while Fig. 4 (b) ($x = 0$) shows a more symmetric distribution. The electric potential close to the metallic objects (IBS cubic body, neutralizer, thruster cases, target debris and back faces of the solar array) adapts locally to the wall potential, in a plasma sheath whose thickness depends on the local plasma density and electron temperature. At the debris surface facing the IBS, the plasma is dense enough to have a Debye length much smaller than the cell size (2 mm versus 4 cm), so that the potential drop occurs in a thin sheath treated outside the PIC model (not shown in the plot) and is smaller than the typical floating wall potential drop, because the ions enter it with hypersonic velocities (the local Mach number is around 50 at the target debris). The back surface of the debris, on the other hand, is clearly non-neutral and the sheath thickness is comparable with the cell size. Fig. 4 (c) shows that the dielectric face of the solar array ($y > 0$) is about 5 V positive with respect to the metallic face, which is grounded. As a consequence, the plasma sheaths are slightly thicker close the conductive face, which therefore draws a positive net current (the dielectric face draws zero net current).

The number density of several particle species of interest are depicted in Fig. 5 (a) to (f). Fig. 5 (a) shows the singly-charged Xe ion density. This is slightly above 10^{15} m^{-3} at the ITT

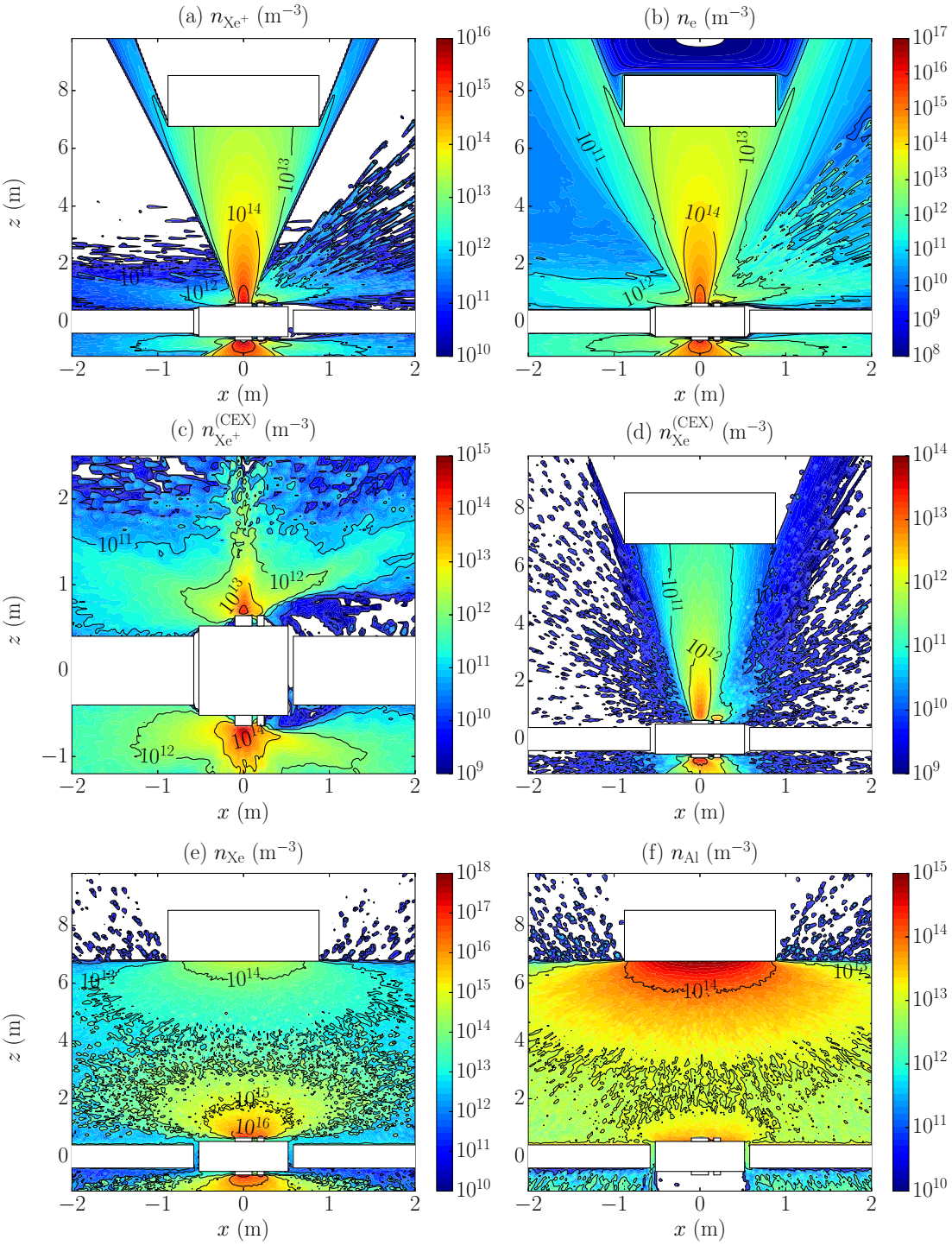

Figure 5: Nominal scenario results: number densities of (a) Xe^+ ions, (b) electrons, (c) Xe^+ ions produced by CEX and ionization collisions (zoomed view, close to the IBS), (d) Xe neutrals produced by CEX collisions, (e) Xe neutrals, and (f) sputtered alluminium neutral atoms.

exit and nearly 10^{16} m^{-3} at the ICT exit. A cloud of slow ions is produced by CEX collisions with a density ranging from 10^{14} m^{-3} at the peripheral plume region to 10^{11} m^{-3} radially outwards. The emitted Xe ions of the neutralizer finally introduce an asymmetry in the near-

region plume properties. Fig. 5 (b) shows the electron density. This presents a similar shape to that of the singly-charged Xe ions, with a few important differences: (I) it drops rapidly very close to the non-neutral IBS surfaces, (II) it is non-zero in the peripheral plume far-region, and (III) it accomodates to the target debris potential in the plasma wake region behind it. The negative charge of these peripheral and plasma wake regions (ions are nearly absent there) is compensated by the positive charge regions that surround the IBS, so that the total net charge in the whole plasma domain is almost zero. Fig. 5 (c) shows the number density of ions produced by collisions in the plume (mostly due to CEX, with a minor contribution of ionization). Peak densities above 10^{14} m^{-3} are reached close to the ITT and ICT thruster exits, while the ions emitted by the neutralizers generate a potential barrier that prevents this ion population from crossing over to the right solar array, at least in the $y = 0$ plane. The fast CEX neutral density is shown in Fig. 5 (d), reaches a peak value slighly downstream of the thruster exit (nearly 10^{13} m^{-3}) and values around 10^{11} m^{-3} at the debris. The Xe neutral density is shown in Fig. 5 (e) and presents values above 10^{17} m^{-3} at the thruster exits, and above 10^{14} m^{-3} at the target debris (due to ion recombination and neutral re-injection).

Fig. 5 (f) shows the sputtered Al atom density, which decreases from almost 10^{15} m^{-3} at the debris to much lower values around 10^{13} m^{-3} close to the IBS surface, where it increases again due to the atoms diffuse reflection. The corresponding particle flux is between 1 and $4 \cdot 10^{16}$ $m^{-2}s^{-1}$ at the IBS front surface, and below 10^{15} $m^{-2}s^{-1}$ at the solar array faces (because of their orientation), with an average impact energy per sputtered atom between 10 and 16 eV (refer to Fig. 2 (b)). Assuming that all Al atoms are adsorbed (worst case for contamination), an average flux of $2 \cdot 10^{16}$ $m^{-2}s^{-1}$, and an IBS mission duration of 170 days with a sunlight orbit fraction of 67%, a contamination layer with a thickness of 3.2 μm would form on all surfaces with a normal along z, enough to affect their operation. Observe that the ambient O^+ flux for the considered scenario is, at normal incidence, $3.75 \cdot 10^{14}$ $m^{-2}s^{-1}$, thus negligible with respect to the backsputtering flux.

The slow Xe^+ (due to near-thruster collisions) and ambient O^+ vector fluxes are shown respectively in Fig. 6 (a) and (b). The CEX ions tend to deviate towards the IBS and radially outwards due to the ambipolar electric field. The emitted ions of the neutralizer prevent these slow ions from crossing over to the right solar arrays, just as observed in Fig. 5 (c). Regarding the ambient O^+ ions, the emitted plume of the ICT acts as a potential barrier (5 – 10 V, as shown in Fig. 4 (a) and (b)) that prevents most of them (which have kinetic energies of about 5 eV) from reaching the IBS cubic body. Moreover, even if they tend to flow around the thin solar arrays, the main plasma plume core of the ITT also rejects them. As a consequence, only a negligible fraction of ambient ions finally hits the target debris.

The total ion current density (due to slow CEX and ambient ions) that reaches the IBS surfaces is shown in Fig. 7 (a) to (d). The maximum current density at the IBS front face (Fig. 7 (a)) is around 0.4 mA/m^2 and is reached close to the neutralizer right corners (the equivalent CEX ion flux is around $2 \cdot 10^{15}$ $m^{-2}s^{-1}$). A similar shape characterizes the back face of the IBS (Fig. 7 (b)), which features a generally larger current density with a peak of more than 1 mA/m^2, since the ICT mass flow rate is larger and the ICT plume features a higher divergence (refer to Table 1). The current flux to the solar arrays (Fig. 7 (c) and (d))

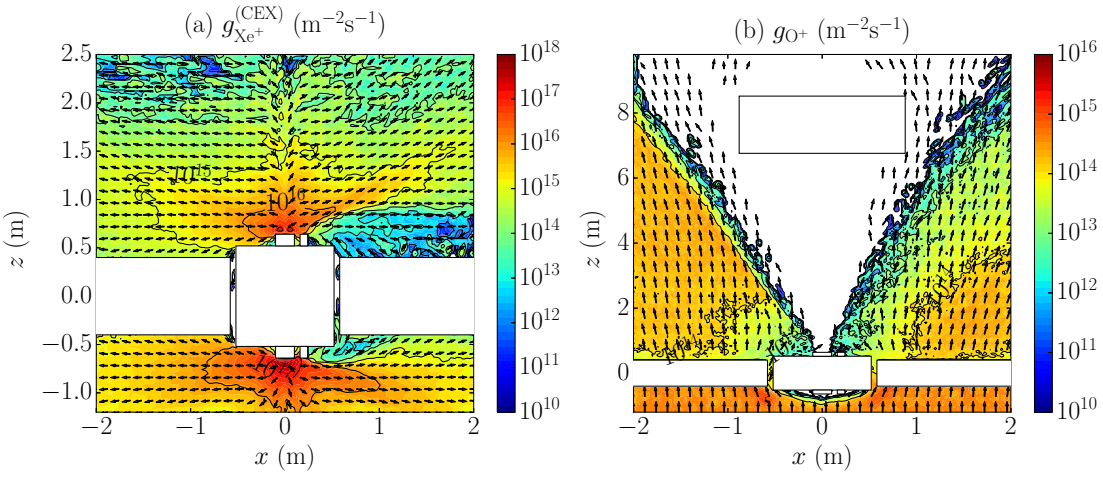

Figure 6: Nominal scenario results at $y = 0$: (a) slow Xe^+ ion vector flux (including ions from both CEX and ionization, but not those injected from the neutralizers), and (b) O^+ ion vector flux. The vector flux direction is shown by the arrows.

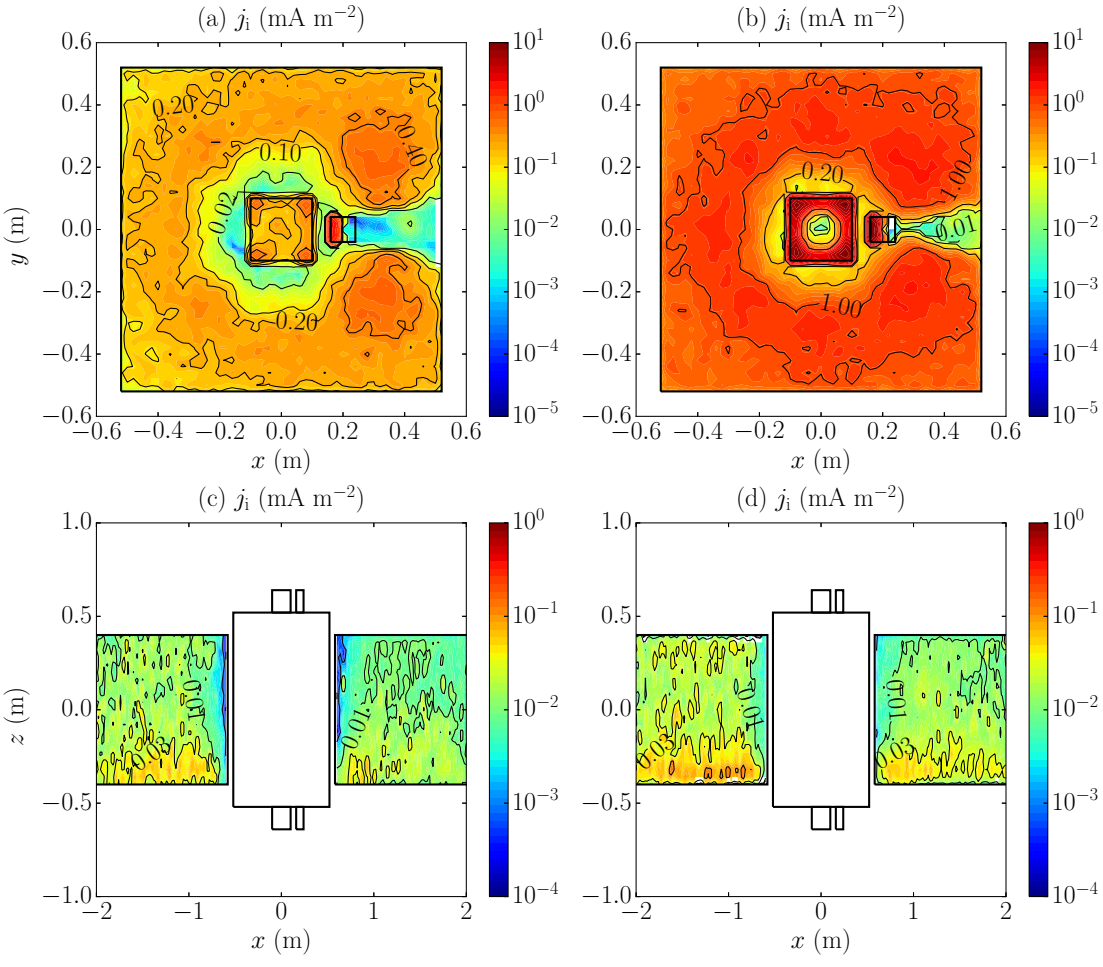

Figure 7: Nominal IBS simulation: total ion current densities to (a) IBS front face (the one facing the debris), (b) IBS back face, (c) dielectric face, and (d) conductive face of the solar arrays.

is 1 or 2 orders of magnitude lower than on the front and back IBS faces, with peaks of 0.05 mA/m^2 on the array side close to the ICT. Moreover, the conductive face of the solar array receives a larger current density, because of its lower electric potential, which attracts a larger fraction of ambient and CEX ions (refer to Fig. 4 (c)). Regarding the CEX ion impact energy, on average, this is between 20 and 30 eV on the front and back IBS faces and on the dielectric face of the solar arrays and between 25 and 35 eV on the conductive face.

The electric potentials of the target debris and of the neutralized ITT plume with respect to the IBS ground and the total ion current to the IBS are provided in Table 2.

Table 2: Electric potential of target debris and neutralized ITT plasma plume (8 cm downstream of the ITT thruster exit) relative to the IBS ground, and total collected ion current by the IBS. Case A: non-nominal simulation with $\gamma = 1.25$; case B: non-nominal simulation with no ambient ions; case C: non-nominal simulation with no collisions; case D: non-nominal simulation with an off-axis target.

	Nominal	**Case A**	**Case B**	**Case C**	**Case D**
ϕ_{plume} (V)	26.3	22.9	26.3	27.8	26.3
ϕ_{target} (V)	9.7	9.9	9.7	11.2	9.5
$I_{\text{i,IBS}}$ (mA)	1.59	1.31	1.46	0.24	1.58

In the nominal simulation, the target debris charges 9.7 V positive relative to the IBS ground, while the neutralized plume (at the location where the electron temperature is fixed to 3 eV) is floating at 26.3 V (this is also known as the coupling voltage of the neutralizer common, which is grounded). The total collected ion current (due to CEX Xe^+ and ambient O^+) is 1.59 mA.

Finally, the transferred force contributions are summarized in Table 3. The predicted contributions for injected singly charged ions is compared with the prediction of the self-similar EASYPLUME model, generalized for non-isothermal ($\gamma > 1$) electrons [12, 11]. A particularly good match is found, with the SSM underestimating slightly the transferred force (1 mN less). In the nominal case, the backsputtered atom contribution is around 3% of the total transferred force, while the effect of recombined Xe neutrals is around 8%. This last contribution is greatly affected by the accommodation coefficient α_{W} (here 0.98), which is typically estimated experimentally and affected by large uncertainties (values between 0.8 and 1 can be found in literature [34, 35]). In particular, the force transferred by recombined neutrals rapidly drops as this coefficient approaches 1, being $\alpha_{\text{W}} = 1$ the most conservative case (lowest force transmission). In this case, the neutral re-injection energy drops from $(1 - \alpha_{\text{W}})\bar{E}_{\text{imp}} \approx 70$ eV (in the nominal case, where $\alpha_{\text{W}} = 0.98$ and $\bar{E}_{\text{imp}} \approx 3600$ eV considers the effect of both singly- and doubly-charged ions) down to $2T_{\text{W}} = 0.0755$ eV (perfect wall accommodation). The transferred force scales as the square root of the re-injection energy (the re-injection flux is constant), so that it drops from 2.67 mN (nominal case) to approx. 0.09 mN ($\alpha_{\text{W}} = 1$). More generally, if we neglect the wall temperature with respect to the re-injection energy, the force contribution of recombined neutrals scales as $\sqrt{1 - \alpha_{\text{W}}}$.

Table 3: The different contributions to the transferred force along z to the target debris, for the considered simulation cases. Case A: non-nominal simulation with $\gamma = 1.25$; case B: non-nominal simulation with no ambient ions; case C: non-nominal simulation with no collisions; case D: non-nominal simulation with an off-axis target. The contribution of the injected Xe^+ ions for the nominal and off-axis target cases is compared with an SSM plume model prediction (given in parenthesis). All force contributions are evaluated at the material wall of the target debris.

	Contributions to the transferred axial force in mN				
	Nominal	**Case A**	**Case B**	**Case C**	**Case D**
Injected Xe^+	28.8(27.7)	29.0	28.8	28.9	22.5(21.2)
Injected Xe^{++}	1.07	1.11	1.07	1.07	0.904
Recombined Xe	2.67	2.70	2.67	2.66	2.08
Fast CEX Xe	0.170	0.173	0.173	0.0	0.147
Sputtered Al	0.934	0.941	0.933	0.934	0.739
Ambient O^+	$1.1 \cdot 10^{-8}$	$1.3 \cdot 10^{-6}$	0.0	$2.0 \cdot 10^{-9}$	$6.3 \cdot 10^{-7}$
Electrons	$7.6 \cdot 10^{-5}$	$8.1 \cdot 10^{-5}$	$7.7 \cdot 10^{-5}$	$7.7 \cdot 10^{-5}$	$2.1 \cdot 10^{-4}$
Electric field	$-9.9 \cdot 10^{-3}$	$-4.8 \cdot 10^{-3}$	$-9.9 \cdot 10^{-3}$	$-1.0 \cdot 10^{-2}$	$-8.4 \cdot 10^{-3}$
Total	33.6	34.0	33.6	33.6	26.3
Fraction of ITT thrust transferred to target	106.7%	107.9%	106.7%	106.7%	83.5%

The contributions of oxygen ions, surface electric fields and electron pressure are finally all negligible. The total force transferred to the debris is above the requirement of 30 mN (it is actually 33.6 mN), which, for a total ITT simulated thrust of 31.5 mN, corresponds to a fraction of ITT thrust transferred to the target of 107% (above 100% due to the recoil effect of recombined Xe and sputtered Al atoms). Finally, the torque is negligible in the nominal case, being $(1.51, 4.55, 0.08)$ μNm.

4. Sensitivity analysis results

In this section we study the sensitivity of the simulation results on some of the simulation parameters and settings. To this puropose, the following set of non-nominal simulations is considered:

- Case A: one simulation with $\gamma = 1.25$ (versus the nominal $\gamma = 1.15$) to study the effects of the electron cooling rate.
- Case B: one simulation without the injection of ambient ions.
- Case C: one simulation without CEX and ionization collisions.

- Case D: one simulation with an off-axis target debris, in which the target center of mass is displaced by +0.44 m along the x direction, and −0.44 m along y.

The electric potentials of target debris and neutralized ITT plume and the transferred force to the target for these 4 non-nominal cases are shown respectively in Tables 2 and 3. Fig. 8 (a) to (c) then show the electric potentials at $y = 0$ for cases A, B and C, while Fig. 8 (d) shows the backsputtering particle flux for case D.

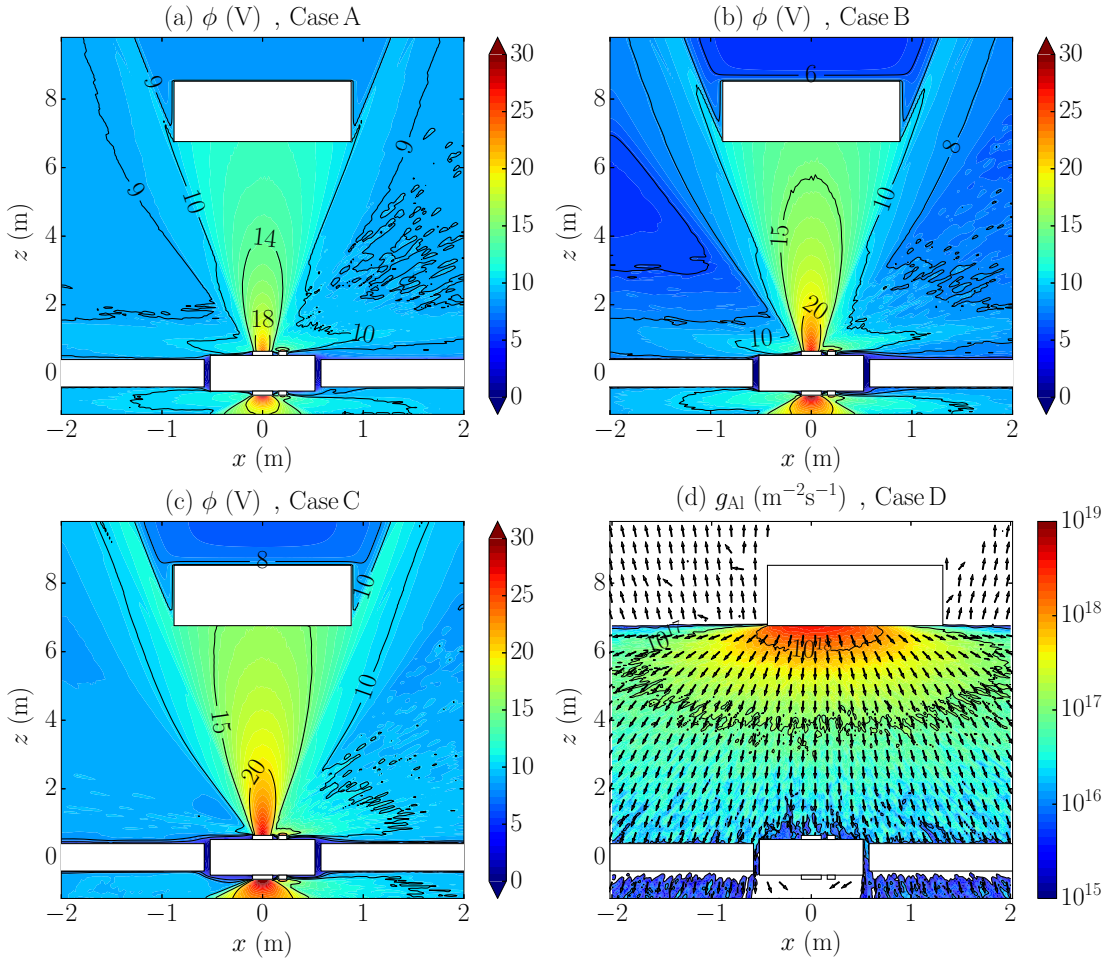

Figure 8: Non-nominal simulation results at $y = 0$: electric potential for (a) case A ($\gamma = 1.25$), (b) case B (no ambient plasma ions), and (c) case C (no collisions). (d) Backsputtering Al atom vector flux for case D (off-axis target debris), with arrows indicating the direction of the vector flux.

4.1. Effects of the electron cooling rate

A parameter of the model which has some uncertainty is the electron polytropic coefficient γ, in $T_{\mathrm{e}} \propto n_{\mathrm{e}}^{\gamma-1}$. Although a more complex functional dependence of the electron temperature on the electron density can be considered, both fully-kinetic simulations, like those of Ref. [31], and experiments suggest that the electron cooling can be reasonably approximated by a polytropic law, with $\gamma \in [1.1, 1.3]$.

The comparison of the electric potential of the nominal case ($\gamma = 1.15$, Fig. 4 (a)) with the non-nominal faster cooling rate case ($\gamma = 1.25$, Fig. 8 (a)), provides important information on the effects of the electron cooling in the plume. A faster cooling yields lower electron temperatures in the expanding plume and consequently lower electric fields. Indeed, as shown in Table 2, a higher electron cooling rate yields a lower difference in potential between the emitting IBS and the neutralized plasma plume (and equivalently, a lower coupling voltage between the neutralizer and the plume). In particular the plume is 22.9 V positive relative to the IBS ground, versus the 26.3 V of the nominal case. Nevertheless, the IBS-target debris relative potential does not change significantly (0.2 V variation), with the target remaining approximately 10 V positive.

The lower ambipolar electric field of the $\gamma = 1.25$ case yields a smaller fraction of slow ions backscattered towards the IBS, as shown in Table 2, where the total ion current collected by the IBS reduces from the nominal 1.59 mA to 1.31 mA.

For what concerns the electron cooling effects on the transferred force to the debris, Table 3 shows that a larger polytropic coefficient yields a slightly larger transferred force to the target (+0.4 mN), because the divergence angle of the emitted ions increases less along the expansion than in the nominal case (smaller ambipolar electric fields). Therefore a slightly larger fraction of emitted ions hits the target debris.

4.2. Effects of the ambient plasma

As shown in Fig. 6 (a) and (b), the IBS emitted plumes act as potential barriers for the ambient plasma ions, so that a negligible fraction of them actually reaches the target debris. For this reason, the simulation with no ambient plasma presents the same transferred force to the debris, as shown in Table 3. The absence of plasma ions reduces the collected ion current by approximately 0.13 mA. This small difference in collected ion current, however, does not affect importantly the neutralized plume potential (relative to the IBS ground) or the neutralizer common coupling voltage, which remains close to the nominal case value (+26.3 V).

Finally, referring to Fig. 8 (b), the electric potential of the no-ambient plasma case drops more rapidly on the sides of the ITT plasma plume, especially on the left side (where the potential is 2V lower approximately). The ambient ions effects are clearly negligible in the rest of the domain.

It can be concluded that ambient ions only play a minor role: their effect is negligible for what concerns the neutralizer coupling voltage and the transferred force to the target, while their total flow to the IBS is approximately 10% of that of the CEX ions, and is almost negligible with respect to the contamination flux of sputtered Al atoms.

4.3. Effects of collisions

The backscattered slow Xe ions, generated by CEX or ionization, represent the most important contribution to the IBS collected ion current. In particular their contribution is one

order of magnitude larger than that of the ambient ions, as shown by the collected current of case C in Table 2. The collected current, in fact, drops from 1.59 mA down to 0.24 mA.

The ions created by collisions in the plume also affect significantly the neutralizer coupling voltage (or the neutralized plume potential with respect to the IBS ground) and the relative target potential. As shown in Table 2, the plume potential increases to 27.8 V when collisions are neglected. This is because, in the absence of CEX ions, no active plasma bridge between neutralized plume and IBS is active, so that the potential difference is higher. Since the target debris potential with respect to the plume is not affected significantly by the near-thruster collisions, the debris potential relative to the IBS also increases up to 11.2 V.

The electric potential in this collisionless scenario (case C) is finally shown in Fig. 8 (c). The main differences with respect to the nominal case (Fig. 4 (a)) are found on the left side of both thrusters, where the absence of CEX ions is evident. On the neutralizers side, on the other hand, the emitted ions mitigate the differences.

Regarding the transferred force to the target, collisions finally play a negligible role, just as expected, given the low collisionality of the plume plasma.

4.4. Effects of the space debris position

When the target debris is off-axis, the symmetry of the backsputtered atom flux with respect to the z axis is lost, as shown in Fig. 8 (d). Nevertheless, this loss of symmetry is almost negligible, at least close to the IBS surfaces in the $y = 0$ plane, so that the contamination flux remains almost unaltered.

The transferred force along z to the debris clearly reduces by 7 mN, from 33.6 to 26.3 mN, since a larger fraction of plume ions misses the target. This corresponds to a fraction of ITT thrust transferred to the target equal to 83.5%. Moreover, the transferred force presents non-negligible components along x and y, being $F_{\text{target},x} = 0.358$ mN and $F_{\text{target},y} = -0.362$ mN. This lateral force is therefore destabilizing as it pushes the target radially outwards, so that the relative position GNC must counteract it.

Finally, the transferred torque to the target debris is no longer negligible (except around the z axis): $(-2.82, -2.82, -6.73 \cdot 10^{-4})$ mN m. This produces an angular momentum build-up in 1 day of approx. 250 kg m^2s^{-1} per axis, which corresponds, for the considered target debris mass and shape, to an angular velocity of approx. 0.3 rad/s. A continuous and constant momentum build-up like this one would induce a rotational velocity of more than 5 Hz at the end of the considered IBS mission (negligible fragmentation risk). Observe, nonetheless, that the relative GNC control, which aims at aligning the ITT with the target center of mass would greatly limit this momentum build up phenomenon.

5. Conclusions

This paper has presented a detailed analysis of a spacecraft-plasma plume-debris interaction in an IBS active debris removal scenario, which has been carried out with the EP2PLUS 3D hybrid code and has permitted evaluating the effects of some of the critical

phenomena affecting this IBS technique. The following conclusions can be drawn.

Firstly, heavy species collisions (occurring mostly close to the thruster exit) generate the well known cloud of slow charge-exchange ions, which are backscattered towards to S/C by the local electric fields. The backscattered ion flux towards the S/C is highest on the back face of the IBS (the one not facing the debris) since the impulse compensation thruster always features a higher mass flow with a higher plume divergence with respect to the impulse transfer thruster. For the mission geometry and specifications considered here, the ion flux on the IBS front face is less than half of the back face flux, while the peak ion current density is 0.4 and 1.0 mA/m^2 for, respectively, the front and back IBS faces. The ion flux on the solar arrays depends on their orientation and, for the considered scenario, is about 2 orders of magnitude smaller than on the front and back IBS faces, with current density peaks of 0.05 mA/m^2. Regarding the mean ion impact energy on the IBS surfaces, this is set by the potential difference between the neutralized plasma plume and the IBS ground (coupling voltage) and is between 20 and 35 eV, a value which should produce negligible surface sputtering, although the confirmation of this statement is left to future studies.

Secondly, the flux of backsputtered aluminium, due to the impingement of hypersonic ions on the target debris surface, produces a non-negligible contamination of the IBS front face. This has been evaluated for an operational shepherding distance of 7 m, a cubic target debris aligned with the plume axis and featuring no special surface covering or finishing. Under such assumptions, an almost homogeneous flux above 10^{16} $m^{-2}s^{-1}$ has been found at the S/C front face, which might dramatically reduce the performance of sensors or solar panels, whose normal is aligned with the debris direction. For the considered mission, a contamination layer of up to 3 μm thickness (worst case scenario) could form during the whole de-orbiting phase (lasting 170 days). Obviously, this contamination flux can be reduced operating at larger distances, at the cost of a lower transferred force. As a rule of a thumb, if the ratio between transferred force and ITT thrust is maintained close to 100% (e.g. by using a lower divergence thruster), the backsputtering flux should reduce with the square of the operational distance, given the nearly spherical expansion of sputtered atoms. Finally, backsputtering atoms impinge the IBS with energies between 10 and 16 eV, so that they should also produce negligible sputtering effects.

Thirdly, the plasma plume of the impulse transfer thruster connects electrically the IBS and the target debris, and determines the stationary difference of potential between the two bodies. Since the target debris is directly exposed to a dense plasma plume (contrary to the IBS, exposed to more rarefied CEX and ambient ions), it generally features a higher potential. For the considered scenario, the target debris charges about 10 V positive, relative to the IBS.

Fourthly, the main contributors to the transferred force to the debris are the singly-charged ions, followed by the recombined Xe neutrals, the emitted doubly-charged ions and the sputtered aluminium atoms. For the considered scenario, Xe^+ accounts for 86% of the total transferred force, while Xe^{++} for 3.2%, the sputtered Al for 2.8% and the recombined Xe for 8.0%. It has also been shown that the recombined Xe contribution strongly depends on the wall accommodation coefficient, which must be determined experimentally, and becomes negligible in the conservative case of perfect accommodation.

A sensitivity analysis has then permitted evaluating the effects of the electron cooling rate, the ambient plasma ions, the heavy species collisions, and an off-axis target debris position. The following has been found:

1. The electron cooling rate in the plasma plume affects the electric potential of the plasma relative to the IBS, but not the relative target potential. Moreover, a higher polytropic coefficient yields a slightly larger transferred force to the target, due to a smaller plume divergence growth, and a lower CEX ion current collected by the IBS.
2. Ambient plasma ions present a minor contribution to the total ion current collected by the IBS (approx. 10%), while the ITT plume prevents most of them from hitting the debris.
3. CEX ions represent the dominant contribution to the IBS collected ion current, and are an important factor in determining also the neutralizer coupling voltage (or the potential of the neutralized plume relative to the IBS ground).
4. An off-axis target position affects only slightly the backsputtered flux on the IBS, although it also causes a significant reduction of the transferred force, the onset of a lateral force, and a non-negligible torque acting on the debris. Both our results and a recent study [7] have shown that the lateral forces, originating due to an off-axis target position, have a destabilizing effect, to be counteracted by the relative position GNC.

Finally, future work shall focus on addressing the effects of some phenomena and mission features that have not been included in this study, such as: (I) non-rectangular and non-aligned space debris objects (affecting both the transferred force and torque, and the backsputtered atoms distribution), (II) Earth magnetic field (affecting the plasma plume expansion), and (III) the sputtering damage on the IBS surfaces.

Acknowledgments

The research leading to the results of this paper was initiated within the *LEOSWEEP* project ("Improving Low Earth Orbit Security With Enhanced Electric Propulsion") and received funding from the European Union Seventh Framework Programme (FP7/2007-2013) under grant agreement N.607457. Additional funding to complete the research has been received by Spain's R&D National Plan, grant ESP2016-75887.

Appendix: Sputtered atoms generation and incident particles treatment

In the PIC module of EP2PLUS, the sputtering effects are considered to be the same independently of the impacting particle charge (be it singly-charged, doubly-charged or neutral). Each impacting macro-particle produces a population of sputtered atoms with a total mass $\Delta m_s = m_s WY$, where m_s is the elementary atomic mass of the target debris material, W is the number weight of the impinging macro-particle (number of elementary particles), and Y the corresponding sputtering yield. The number of sputtered macro-particles and their weight are given by a population control algorithm, described in Ref. [16], which maintains

their number per cell within a desired interval. Regarding the velocity distribution of sputtered atoms, this is assumed to be given by a semi-Maxwellian injection from a thermal reservoir (of zero fluid velocity and temperature $\bar{E}_\mathrm{s}/2$), so that the probability of injecting a sputtered macro-particle with a velocity $\boldsymbol{v}$ goes as [33]:

$$f_\mathrm{s}(\boldsymbol{v}) \propto v_\perp \exp\left(-\frac{m_\mathrm{s} v^2}{\bar{E}_\mathrm{s}}\right), \tag{4}$$

where $v_\perp$ is the emission velocity normal component with respect to the material surface. This is a clearly a simplifying assumption, because the distribution can be asymmetric with respect to the surface normal, and generally depends on both the impact angle and the principal directions of the sputtered material lattice [36, 37].

Coming to the impinging particle, of elementary mass m, it can either be quickly backscattered (with probability p_b) or suffer a partial/complete accommodation process. If the macro-particle is backscattered, it is specularly reflected with a reduced energy

$$E_\mathrm{b} = (1 - C_\parallel)\,\bar{E}_\mathrm{s} + C_\parallel \left(E_\mathrm{i} - Y\bar{E}_\mathrm{s}\right), \tag{5}$$

with

$$C_\parallel = \left[\frac{\alpha_\mathrm{i} - \alpha_\mathrm{min}}{\pi/2 - \alpha_\mathrm{min}}\right]^\beta, \tag{6}$$

where β is an empirical coefficient (determined from either SRIM/TRIM simulations or experiments), and α_min is the minimum impact angle that yields a non-zero backscattering probability (in the simulations of Sec. 3, $\beta = 4$ and $\alpha_\mathrm{min} \approx 50$ deg). Eq. (5) contains the most important dependencies of the backscattered particle energy. As $\alpha_\mathrm{i} \to \pi/2$ (parallel incidence), and hence $C_\parallel \to 1$, the particle tends to conserve most of its kinetic energy E_i, since it barely enters the material lattice. Nevertheless, it loses some energy due to having produced the sputtered atoms, that is $Y\bar{E}_\mathrm{s}$. Secondly, as $\alpha_\mathrm{i} \to \alpha_\mathrm{min}$, the particle tends to be backscattered with the same energy as the rest of the sputtered atoms. This approach is another simplification of the real physics for two reasons: (I) the actual backscattering direction does not coincide exactly with the specular reflection direction (but it is narrowly distributed around it), and (II) the backscattered particles, of a given impact energy and angle, have some energy spread, rather than a single energy, as considered here.

If the macro-particle is not backscattered within the first atomic layers, it enters deeply the material and suffers a large number of collisions with the lattice atoms. As a result, it gradually reaches a thermodynamic equilibrium with the wall, at temperature T_W, and, if it is an ion, it also recombines with a wall electron. Once it is finally re-emitted, the particle kinetic energy is, on average:

$$\bar{E}_\mathrm{r} = \alpha_\mathrm{W} 2T_\mathrm{W} + (1 - \alpha_\mathrm{W})\bar{E}_\mathrm{i}, \tag{7}$$

where α_W is an energy accommodation coefficient [33, 34, 35], controlling the degree of accommodation (1 for a perfect accommodation), and $\bar{E}_\mathrm{i}$ is the mean impact energy of the impacting particle population. Finally, the re-injection probability follows Eq. 4 with the substitutions $\bar{E}_\mathrm{s} \to \bar{E}_\mathrm{r}$ and $m_\mathrm{s} \to m$.

References

[1] D.J. Kessler, N.L. Johnson, J.C. Liou, and M. Matney. The Kessler syndrome: implications to future space operations. In *AAS Guidance and Control Conference*, paper 2010-016. American Astronautical Society, Springfield, VA, 2010.

[2] J.C. Liou and N.L. Johnson. A sensitivity study of the effectiveness of active debris removal in LEO. *Acta Astronautica*, 64(2):236–243, 2009.

[3] J.C. Liou, N.L. Johnson, and N.M. Hill. Controlling the growth of future LEO debris populations with active debris removal. *Acta Astronautica*, 66(5):648–653, 2010.

[4] L. Jasper, P. Andersony, H. Schaubz, and D. McKnight. Economic and risk challenges of operating in the current space debris environment. In *3rd European Workshop on Space Debris Modeling and Remediation*, Paper 8.2, CNES, Paris, France, 2014.

[5] C. Bombardelli and J. Peláez. Ion beam shepherd for contactless space debris removal. *Journal of Guidance, Control, and Dynamics*, 34(3):916–920, 2011.

[6] C. Bombardelli and J. Peláez. Ion beam shepherd for asteroid deflection. *Journal of Guidance Control and Dynamics*, 34(4):1270, 2011.

[7] C. Bombardelli, H. Urrutxua, M. Merino, E. Ahedo, and J. Peláez. Relative dynamics and control of an ion beam shepherd satellite. In *Advances in the Astronautical Sciences, proceedings of Space Flight Mechanics conference 2012*, volume 143, pages 2145–2158. Univelt, Inc., 2012.

[8] C. Bombardelli, H. Urrutxua, M. Merino, E. Ahedo, and J. Peláez. The ion beam shepherd: A new concept for asteroid deflection. *Acta Astronautica*, 90(1):98–102, 2013.

[9] M. Merino, E. Ahedo, C. Bombardelli, H. Urrutxua, and J. Peláez. Ion beam shepherd satellite for space debris removal. In *Progress in Propulsion Physics*, volume 4 of *EUCASS Advances in Aerospace Sciences*, pages 789–802. EDP Sciences, Les Ulis, France, 2013.

[10] F. Cichocki, M. Merino, and E. Ahedo. Modeling and simulation of EP plasma plume expansion into vacuum. In *50th Joint Propulsion Conference*, paper 2014-3828, Cleveland, Ohio, July 28-30, 2014. AIAA, Reston, VA.

[11] M. Merino, F. Cichocki, and E. Ahedo. Collisionless plasma thruster plume expansion model. *Plasma Sources Science and Technology*, 24(3):035006, 2015.

[12] F. Cichocki, M. Merino, E. Ahedo, D. Feili, and M. Ruiz. Electric propulsion subsystem optimization for "Ion Beam Shepherd" missions. In *34th International Electric Propulsion Conference*, paper 2015-420, Hyogo-Kobe, Japan, July 6-10, 2015. Electric Rocket Propulsion Society, Fairview Park, OH.

[13] F. Cichocki, M. Merino, E. Ahedo, M. Smirnova, A. Mingo, and M. Dobkevicius. Electric propulsion subsystem optimization for "Ion Beam Shepherd" missions. *Journal of Propulsion and Power*, 33(2):370–378, 2017.

[14] M. Ruiz, I. Urdampilleta, C. Bombardelli, E. Ahedo, M. Merino, and F. Cichocki. The FP7 LEOSWEEP project: Improving low Earth orbit security with enhanced electric propulsion. In *Space Propulsion Conference*, paper 2014-2980908, Cologne, Germany, May 19-22, 2014. 3AF, Paris, France.

[15] F. Cichocki, A. Domínguez, M. Merino, and E. Ahedo. A 3D hybrid code to study electric thruster plumes. In *Space Propulsion Conference*, paper 2016-3124968, Rome, Italy, May 2-6, 2016. 3AF, Paris, France.

[16] F. Cichocki, A. Domínguez, M. Merino, and E. Ahedo. Hybrid 3D model for the interaction of plasma thruster plumes with nearby objects. *Plasma Sources Science and Technology*, 26(12):125008, 2017.

[17] F. Cichocki. *Analysis of the expansion of a plasma thruster plume into vacuum*. PhD thesis, Universidad Carlos III de Madrid (UC3M), Leganés, Spain, 2017.

[18] K. Dannenmayer, S. Mazouffre, E. Ahedo, and M. Merino. Hall effect thruster plasma plume characterization with probe measurements and self-similar fluid models. In *48th Joint Propulsion Conference and Exhibit*, paper 2012-4117, Atlanta, Georgia, July 30 - August 1, 2012. AIAA, Reston, VA.

[19] J.E. Foster, G.C. Soulas, and M.J. Patterson. Plume and discharge plasma measurements of an NSTAR-type ion thruster. In *36th Joint Propulsion Conference and Exhibit*, paper 2000-3812, Huntsville, Alabama, July 16-19, 2000. AIAA, Reston, VA.

[20] B.E. Beal, A. Gallimore, W.A. Hargus, and J.M. Haas. Plasma properties in the plume of a Hall thruster cluster. *Journal of Propulsion and Power*, 20(6):985–991, 2004.

[21] B.E. Beal, A. Gallimore, and W.A. Hargus. Plasma properties downstream of a low-power Hall thruster. *Physics of plasmas*, 12(12):123503, 2005.

[22] L. Brieda, M.R. Nakles, D.R. Garrett, W.A.Jr. Hargus, and R.L. Spicer. Experimental and numerical examination of the BHT-200 Hall thruster plume. In *30th International Electric Propulsion Conference*, paper 2007-73, Florence, Italy, September 17-20, 2007. Electric Rocket Propulsion Society, Fairview Park, OH.

[23] R.M. Myers and D.H. Manzella. Stationary plasma thruster plume characteristics. In *23rd International Electric Propulsion Conference*, paper 1993-096, Seattle, Washington, September 13-16, 1993. Electric Rocket Propulsion Society, Fairview Park, OH.

[24] L.B. King and A.D. Gallimore. Ion-energy diagnostics in the plasma exhaust plume of a Hall thruster. *Journal of Propulsion and Power*, 16(5):916–922, 2000.

[25] S.K. Absalamov, V.B. Andreev, T. Colbert, M. Day, V.V. Egorov, R.U. Gnizdor, H. Kaufman, V. Kim, A.I. Koriakin, and K.N. Kozubskii. Measurement of plasma parameters in the stationary plasma thruster (SPT-100) plume and its effect on spacecraft components. In *28th Joint Propulsion Conference and Exhibit*, paper 1992-3156, Nashville, Tennessee, July 6-8, 1992. AIAA, Reston, VA.

[26] A. Cohen-Zur, A. Fruchtman, and A. Gany. The effect of pressure on the plume divergence in the Hall thruster. *IEEE Transactions on Plasma Science*, 36(5):2069–2081, 2008.

[27] J. Wang, O. Chang, and Y. Cao. Electron-ion coupling in mesothermal plasma beam emission: Full particle PIC simulations. *IEEE Transactions on Plasma Science*, 40(2):230–236, 2012.

[28] J. Wang, D. Han, and Y. Hu. Kinetic simulations of plasma plume potential in a vacuum chamber. *IEEE Transactions on Plasma Science*, 43(9):3047–3053, 2015.

[29] F. Cichocki, M. Merino, E. Ahedo, Y. Hu, and J. Wang. Fluid vs PIC modeling of a plasma plume expansion. In *34th International Electric Propulsion Conference*, paper 2015-035, Hyogo-Kobe, Japan, July 6-10, 2015. Electric Rocket Propulsion Society, Fairview Park, OH.

[30] M. Martínez-Sánchez, J. Navarro-Cavallé, and E. Ahedo. Electron cooling and finite potential drop in a magnetized plasma expansion. *Physics of Plasmas*, 22(5):053501, 2015.

[31] M. Merino, J. Mauriño, and E. Ahedo. Direct-Vlasov study of electron cooling mechanisms in paraxial, unmagnetized plasma thruster plumes. In *35th International Electric Propulsion Conference*, paper 2017-104. Electric Rocket Propulsion Society, Fairview Park, OH, 2017.

[32] L.A. Giannuzzi et al. *Introduction to focused ion beams: instrumentation, theory, techniques and practice*. Springer Science & Business Media, 2006.

[33] O.V. Sazhin, S.F. Borisov, and F. Sharipov. Accommodation coefficient of tangential momentum on atomically clean and contaminated surfaces. *Journal of Vacuum Science & Technology A: Vacuum, Surfaces, and Films*, 19(5):2499–2503, 2001.

[34] R. Santos. *Código híbrido avanzado de motores de plasma de efecto Hall*. PhD thesis, Universidad Politécnica de Madrid (UPM), Madrid, Spain, 2012.

[35] V.J. Murray, M.D. Pilinski, E.J. Smoll Jr, M. Qian, T.K. Minton, S.M. Madzunkov, and M.R. Darrach. Gas–surface scattering dynamics applied to concentration of gases for mass spectrometry in tenuous atmospheres. *The Journal of Physical Chemistry C*, 121(14):7903–7922, 2017.

[36] Y. Yamamura. Theory of sputtering and comparison to experimental data. *Nuclear Instruments and Methods in Physics Research*, 194(1-3):515–522, 1982.

[37] P. Sigmund. Recollections of fifty years with sputtering. *Thin Solid Films*, 520(19):6031–6049, 2012.

[38] J.F. Ziegler, M.D. Ziegler, and J.P. Biersack. SRIM - The stopping and range of ions in matter (2010). *Nuclear Instruments and Methods in Physics Research B*, 268(11-12):1818–1823, 2010.

[39] A. Alpatov, F. Cichocki, A. Fokov, S. Khoroshylov, M. Merino, and A. Zakrzhevskii. Determination of the force transmitted by an ion thruster plasma plume to an orbital object. *Acta Astronautica*, 119:241–251, 2016.

[40] J. D. Jackson. *Classical electrodynamics*. American Association of Physics Teachers, College Park, MD, 1999.